Title

High-throughput synapse profiling reveals cell-type-specific spatial configurations in the fly brain

Authors

Hongyang Wu[1], Yoh Maekawa[2], Sayaka Eno[1], Shu Kondo[3], Nobuhiro Yamagata[1,4], Hiromu Tanimoto[1,2]*

Affiliations

[1] Graduate School of Life Sciences, Tohoku University, Sendai, Japan.

[2] Department of Biology, Faculty of Science, Tohoku University, Sendai, Japan.

[3] Department of Biological Science and Technology, Tokyo University of Science, Tokyo, Japan.

[4] Department of Life Science, Graduate School of Engineering Science, Akita, Akita University.

* Correspondence: Dr. Hiromu Tanimoto (hiromut@m.tohoku.ac.jp)

Abstract

Characterization of intracellular synapse heterogeneity aides to understand the intricate computational logic of neuronal circuits. Despite recent advances in connectomics, the spatial patterns of synapses and their inter-individual variability remain largely unknown. Using directed split-GFP reconstitution, we achieved visualization of endogenous Bruchpilot (Brp), a presynaptic active zone (AZ) scaffold protein, in a cell-type-specific manner. By developing a high-throughput quantification pipeline, we profiled AZ structures in identified neurons of the mushroom body circuit, where intracellular synaptic patterns are crucial due to compartmentalized connectivity. Quantitative characterization of the pattern of Brp clusters across multiple individuals revealed cell-type-dependent synapse heterogeneity and stereotypy. Furthermore, we discovered previously unidentified sub-compartmental synapse configuration and its transient structural plasticity triggered by associative learning. Synapse profiling thus uncovered multi-layered organizations of AZs, ranging from neighboring synapses to consistent patterns across individuals.

Keywords:

Intracellular synaptic configuration; synapse profiling; active zones; Bruchpilot; mushroom body circuit; split-GFP; synapse heterogeneity; synapse stereotypy; structural plasticity; associative learning

Introduction

40 The brain is a complex network of neurons, and understanding their wiring strategies
41 provides crucial insights into their roles in neuronal computation. Release sites in the
42 presynaptic terminal of *Drosophila* neurons are decorated with electron-dense projections
43 composed of the active-zone (AZ) scaffold protein Brp [1–7]. These Brp projections serve as a
44 synapse marker enabling the whole-brain connectomes, comprehensive mapping of
45 synaptic connections at the electron microscopic level [8–12]. While connectome-based
46 approaches catalyzed the exploration of cell type distinctions, circuit motifs, and
47 neurotransmitters, their application to comparisons across different conditions is still
48 challenging due to the limited throughput of data acquisition and dense reconstruction.
49 Since the synaptic structure and connectivity reflect substantial variability of development
50 and experiences [11,13–18], cross-individual comparisons are necessary. Fluorescence labeling
51 offers high throughputs and contents, especially when comparing synaptic organizations
52 across cell-types [19] or brain regions [20]. Nevertheless, characterizing endogenous synapses in
53 specific cells using fluorescence-labeling remains challenging in the central nervous system
54 (CNS) due to the dense synaptic connections from different neurons. This has driven
55 growing interest in designing cell-type-specific fluorescence-tagging strategies for
56 endogenous synaptic protein [21].

57 The circuit of *Drosophila* mushroom bodies (MBs) plays a central role in olfactory
58 associative learning [22]. The major intrinsic MB neuron, known as Kenyon cells (KCs)
59 respond to odor stimulation and synapse onto the spatially segregated dendrites of MB
60 output neurons (MBONs) that divide the MB into compartments. Distinct types of
61 dopaminergic neurons (DANs) synapse onto specific compartments and thereby modulate

62 KC-MBON synapses in the corresponding compartments [23]. Presynaptic calcium levels of
63 these DANs undergo sub-compartmental GABAergic modulation and inform memory
64 specificity, postulating the distinct synapse structures at individual release sites [24] . Two
65 types of giant interneurons, the anterior paired lateral neuron (APL) and the dorsal paired
66 medial (DPM) neuron extensively ramify across the MB lobes and provide recurrent
67 modulations to KC synapses [25–32]. Considering their comprehensive projections throughout
68 the MB lobes, the modulation of local circuits requires intracellular synaptic tuning. These
69 studies together underscore the importance to spatially distinguish individual synapses
70 within a cell. However, the high AZ density in the MB lobes precluded conventional
71 approaches of fluorescent microscopy from profiling synaptic structures of specific neurons
72 [9].

73 Here, we present a spatial analysis of individual AZs within the MB circuit at the
74 single-cell resolution, achieved by cell-type-specific visualization of endogenous Brp using
75 the CRISPR/Cas9-mediated split-GFP tagging system. We developed a high-throughput
76 quantification pipeline to systematically profile Brp clusters of individual AZs in different
77 MB-innervating neurons. Characterizing multiple structural parameters revealed a
78 significant synaptic heterogeneity within single neurons and AZ distribution stereotypy
79 across individuals. These cell-type-specific synapse profiles suggest that AZs are organized
80 at multiple scales, ranging from neighboring synapses to across individuals.

81

82 **Results**

83 **Establishing an experimental system for cell-type-specific profiling of active zone**
84 **structures**

85 As the molecular assembly of synapses is reported to be sensitive to the dosage of Brp, we
86 visualized endogenous Brp instead of transgenic expression of tagged Brp [33]. To label
87 endogenous Brp specifically in designated cell types, we employed the split-GFP tagging
88 system [34,35] . Using CRISPR/Cas9, we inserted the GFP_{11} fragment (the eleventh β-strand
89 of the super-folder GFP) just prior to the stop codon of *brp* gene. The GFP_{1-10} fragment is
90 expressed in cells of interest by the GAL4/UAS system. The self-assembly of the split-GFP
91 fragments is therefore directed only in GAL4-expressing cells and visualizes endogenous
92 Brp through reconstituted GFP fluorescence (Fig. 1A). As a proof of principle, we directed
93 GFP reconstitution and expressed a plasma membrane marker in the single serotonergic
94 DPM neuron using *VT64246-GAL4* (Fig. 1B). Confocal microscopy revealed
95 Brp::reconstituted GFP (Brp::rGFP) signals only to the MB lobes, aligning with DPM
96 terminals [32]. These signals were distributed as discrete puncta within plasma membrane
97 varicosities resembling presynaptic boutons (Fig. 1B), suggesting that Brp::rGFP clusters
98 labeled individual AZs in the DPM neuron.

99 To systematically profile Brp::rGFP clusters, we developed an image processing
100 pipeline (Fig. 1A). In brief, image deconvolution was applied to reduce out-of-focus light
101 and enhance signal sharpness. Individual Brp::rGFP clusters were then segmented using the
102 3D suite plugin in Fiji [36], generating the 3D region-of-interests (3D ROIs) that encircle each
103 cluster. Brp::rGFP signal intensity, volume and location of individual clusters were
104 measured using the 3D ROIs. To optimize the segmentation, we systematically varied the

105 parameters and calculated the F-score to measure detection accuracy against manually
106 defined ground truth (see Materials and Methods). The F-score is near 1.0 in segmenting
107 Brp::rGFP clusters within DPM and APL neurons and achieved > 0.90 in KCs with certain
108 combinations of segmentation parameters (Fig. 1B).

109 To confirm that Brp puncta represent AZs, we quantified the numbers of Brp::rGFP
110 clusters in DPM and APL neurons specifically and compared them to the connectome data.
111 We found that cluster counts closely matched the number of AZs annotated by the
112 hemibrain connectome (Fig. 1C) [9]. This result validated our method that accurately isolated
113 Brp::rGFP clusters corresponding to single AZs.

114

115 **AZ profiles within KCs are compartmentally heterogeneous**

116 Brp accumulation at individual AZs is known to be heterogeneous even within a single
117 motor neuron [5,6,37,38]. To study such AZ heterogeneity in CNS neurons, we quantified the
118 signal intensity of individual Brp::rGFP clusters in MB lobes. Using KC subtype-specific
119 drivers to direct split-GFP reconstitution in γ KC (*MB009B-GAL4*), α'/β' KCs (*MB370B-*
120 *GAL4*) and α/β KCs (*MB008B-GAL4*). we found that within-cluster Brp::rGFP intensities
121 are highly diverse in all KC subtypes (Fig. 2A).

122 To visualize spatial patterns of Brp::rGFP intensity in each KC subtype, we
123 reconstructed 3D distribution of Brp::rGFP clusters and color-coded them by signal
124 intensities (Fig. 2B). We found that clusters showed noticeable intensity differences
125 between compartments in all subtypes. Even adjacent compartments such as γ1 and γ2, β'2
126 and β'1, α2 and α3, showed drastic differences (Fig. 2B). Importantly, these compartmental

127 patterns were stable across individuals (Fig. 2C) [39]. This result suggests that AZs in
128 different compartments have distinct structures. Since individual KCs of each subtype
129 synapse onto all compartments [8–10,40], this Brp compartmental heterogeneity is likely
130 formed intracellularly.
131

132 **Intracellular heterogeneity of Brp concentration at individual AZs and cell-type**
133 **dependent diversity**

134 Super-resolution microscopy has shown that the Brp molecular density at individual AZs is
135 dynamically adjusted in motor neurons [41,42]. We hypothesized that the amount of Brp does
136 not necessarily correlate with AZ cluster size. To verify this, we calculated the Brp
137 concentration by quantifying both the volume (number of voxels within a 3D ROI) and the
138 Brp::rGFP intensity of each cluster. We found that clusters with similar sizes can exhibit
139 vastly different signal intensities in the DPM neuron, suggesting the heterogeneity of Brp
140 concentration at individual AZs (Fig. 3A). Correlation analysis between the Brp::rGFP
141 intensity and cluster volume revealed a substantial variability among cell types (Fig. 3B-E).
142 There were even significant differences among KC subtypes. These results suggest cell-
143 type dependent variability of the Brp concentration of individual clusters.
144

145 **Stereotypy of intracellular distribution of AZs**

146 To study the spatial distribution of Brp clusters within single neurons, we focused on
147 DANs. *MB504B-GAL4* labels four types of single PPL1 DANs projecting to distinct
148 compartments [43]. Using this driver, we analyzed Brp::rGFP distribution in each

149 compartment and found it uneven in terminals of both PPL1-α2α'2 and α3 (Fig. 4A-B). To
150 better characterize cluster distribution, we calculated the "AZ density" defined as the
151 number of Brp::rGFP clusters surrounding a particular cluster within a specified radius (see
152 Fig. 1A and Materials and Methods for detail). By color-coding Brp::rGFP clusters
153 according to their AZ density, we found that AZs in PPL1-α3 were more localized to the
154 core of the α3 compartment. This pattern was consistent across individuals (Fig. 4C-D),
155 suggesting a stereotyped AZ distribution within PPL1-α3 neurons.

156 We extended the analysis to two other single pairs of neurons innervating the MBs,
157 the DPM and APL neurons. Visualizing AZ density revealed a stereotyped and
158 compartment specific distribution in the DPM neuron (Fig. 5A). Specifically, the AZ
159 density was constantly high in the α'/β' lobes across all individuals, supporting the known
160 functional importance of DPM branches in the α'/β' lobes [30]. In contrast, this compartmental
161 pattern was less pronounced in the APL neuron. Notably, the ratio of AZ density between
162 α3 and α'3 is strikingly different among individuals (Fig. 5B). Taken together, these data
163 suggest that the individual variability in AZ distribution depends on the cell type.
164

165 **Regulation of spatial configuration of AZs**

166 Characteristics of Brp clusters and AZ distribution in KCs revealed spatial
167 organization at the level of compartments. Recent studies further showed intra-
168 compartmental variability of synaptic plasticity upon associative learning, prompting us to
169 analyze sub-compartmental organization of AZs [44,45]. We thus examined potential local
170 patterns among AZs in proximity by calculating the correlation between nearest neighbor

171 clusters in terms of their Brp::rGFP intensities. This analysis revealed strong correlations in
172 KCs and APL but not in DPM (Fig. 6A).

173 We further analyzed the sub-compartmental AZ patterns by examining the spatial
174 distribution of Brp::rGFP intensity. To reduce the high frequency variability of Brp::rGFP
175 intensities (Fig. 2B), we calculated the "local intensity" for each cluster by applying mean
176 filtering (the average Brp::rGFP intensity of all surrounding clusters within a specified
177 radius *r*, see Materials and Methods for detail). By visualizing the local intensity in γ KCs,
178 we identified AZ "hot spots", sub-compartment-sized small groups of AZs with high local
179 intensities, on top of the compartmental differences (Fig. 6B). Since Brp molecules are
180 clustered more in AZ-dense boutons of a single motor neuron [5], we hypothesized that these
181 hot spots correspond to regions with higher AZ densities. Indeed, we found that hot spots
182 appear in high AZ densities regions in γ KCs (Fig. 6B). Consistently, correlation between
183 the local intensity and the AZ density was high in all KC subtypes. In contrast, for DPM
184 and APL neurons, the local intensity of Brp::rGFP was not associated with AZ density (Fig.
185 6C-D). Taken together, these results suggest previously unidentified sub-compartmental
186 synaptic configuration organized across individual KCs.

187

188 **Associative learning re-organizes sub-compartmental synaptic configuration**

189 Sub-compartmental synaptic configuration may undergo experience-dependent
190 changes, such as through associative learning [17,18]. To examine such structural plasticity,
191 we visualized Brp::rGFP specifically in KCs using *R13F02-GAL4* (Fig. 7A) and presented
192 flies with odor (4-methylcyclohexanol) with a concomitant (paired) or shifted (unpaired)

193 electric shock (Fig. 7B). The difference between the paired and unpaired groups therefore
194 represents the effect of associative learning. We prepared the brains at different time points
195 (ranging from 3 min to 1 day) after conditioning and measured the correlation between the
196 AZ density and local intensity of individual Brp::rGFP clusters. Strikingly, we found that
197 associative learning induced a transient modification to the KC synaptic configurations in a
198 compartment-specific manner (Fig. 7C). This learning-induced structural plasticity was
199 specific at 90 min after conditioning and disappeared within one day (Fig. 7D), consistent
200 with previous studies reporting short-lived AZ remodeling in the MBs by conditioning [17,18].
201 These results showcase the advantage of split-GFP system in reporting the dynamics of
202 local synapse subsets with high throughputs and contents. Altogether, we suggest that
203 associative learning induces transient memory traces of local structural plasticity in AZ
204 configuration.
205

206 **Discussion**

207 By leveraging the CRISPR/Cas9 genome editing and split-GFP technique, we
208 systematically profiled presynaptic structures of MB neurons in a cell-type-specific
209 manner. This approach enabled high-throughput analysis of multiple brain samples and
210 detailed characterizations, revealing previously inaccessible structural features of AZs in
211 CNS neurons.

212 Single-cell level analysis of AZ profiles revealed cell-type-specific stereotypy in
213 spatial regulation (Fig. 4-6). We found that AZ density in the DPM neurons is consistently
214 high in the α'/β' lobes across individuals (Fig. 5). This AZ stereotypy of DPM explains the

215 functional significance of the branches in the α'/β' lobes. Overexpression of a Down
216 syndrome cell adhesion molecule (DScam) variant in the DPM neurons was shown to
217 disrupt their innervation except in the α'/β' lobe, while memory formation remained
218 unaffected [30]. Similarly, our analysis identified the intracellular stereotypy in AZ
219 distribution of the PPL1-α3 DAN within the α3 compartment (Fig. 4). This sub-
220 compartmental organization of the single DAN and layered projections of α/β KCs may
221 underlie the differential dopaminergic modulation of KC subtypes in associative learning [46].
222 While such stereotypy is less pronounced in APL, we found strong correlations between
223 Brp::rGFP intensities of neighboring AZs in contrast to DPM (Fig. 6D). This suggests that
224 AZs in APL neurons are organized more locally, allowing them to modulate microcircuits
225 composed of KCs, DANs and MBONs [47]. Collectively, the spatial scale of AZ
226 organizations depends on cell types, reflecting the function of individual MB neurons.
227 We observed that Brp::rGFP intensity correlates strongly with the AZ size in KC
228 subtypes, in contrast to DPM and APL neurons (Fig. 3). Previous studies using localization
229 microscopy showed that the molecular density of synaptic proteins at AZs can be
230 dynamically adjusted in motor neurons, potentially modulating the synaptic vesicle release
231 [41,42,48]. The variable Brp concentrations (i.e. the ratio of the Brp::rGFP intensity to the AZ
232 size) in DPM and APL neurons may represent AZs with distinct Brp densities and therefore
233 different functional modes (Fig. 3) [41]. Notably, a recent study successfully predicted the
234 neurotransmitter type of neurons using the ultrastructure of dense projections as one of the
235 parameters [49], suggesting neurotransmitter-specific AZ structures. Interestingly, both the
236 DPM and APL neurons are reported to release multiple neurotransmitters [27,31,50–53]. Distinct

237 Brp concentrations at AZs might thus support particular release modes or neurotransmitter
238 types.

239 In KCs, the spatial analysis of local AZ configuration revealed strong correlations
240 between Brp::rGFP intensities at neighboring AZs as well as AZ "hot spots", regions with
241 high Brp localization and AZ densities (Fig. 6). These results suggest previously
242 unidentified, highly localized sub-compartmental AZ structures, which are likely organized
243 across individual KCs. Presynaptic terminals of a single KC are found to be highly
244 heterogeneous in terms of their plasticity upon dopamine modulation and associative
245 learning [44,45]. A recent study found the sub-compartmentally heterogeneous activities of
246 dopamine terminals explain memory specificity [24]. Such locally distinct dopamine input
247 may be a source of the AZ hot spot formation in KC terminals. This model is consistent
248 with the localization of two opposing dopamine receptors Dop1R1 and Dop2R to AZs [54].
249 Furthermore, we showed that the local configuration undergoes structural plasticity upon
250 associative learning that involves presynaptic dopaminergic modulation [55–60] (Fig. 7). Since
251 cAMP signaling plays a crucial role in the AZ structural plasticity especially during
252 associative memory formation [39,48,61], it may underlie learning-induced plasticity in sub-
253 compartmental AZ configuration [17,18].

254 **Materials and Methods**

255 **Animals**

256 Flies were maintained on standard cornmeal food at 25 °C under a 12:12 h light-dark cycle
257 for all experiments. All flies used for experiments are 3-7 days old adult males. Flies were
258 transferred to fresh food vials after hatching and flipped every two days before
259 experiments. The GAL4-UAS system was used to express transgenes, and balancers were
260 removed for animals used in all experiments. Fly strains and resources used in this study
261 are as follow: *MB008B-GAL4* (BDSC 68291) [23], *MB009B-GAL4* (BDSC 68292) [23];
262 *MB370B-GAL4* (BDSC 68319) [23], *MB504B-GAL4* (BDSC 68329) [23] , *VT64246-GAL4*
263 (VDRC 204311) [62], *GH146-GAL4* (BDSC 30026) [63], *R58E02-GAL4* (BDSC 41347) [64],
264 *R13F02-GAL4* (BDSC 48571) [64] , *UAS-CD4::tdTomato* (BDSC 35841, by Dr. Yhu Nung
265 Jan & Chun Han), [59]*brp::GFP*$_{11}$ [39], *UAS-GFP*$_{1-10}$ [35].

266

267 **Single-odor aversive conditioning**

268 Adult flies at 3-7 days after eclosion were kept in a 25 °C incubator before and after
269 conditioning. Approximately 50 flies were put in a training tube that is set inside the
270 climate box for 2 minutes before the conditioning. Temperature in the climate box was set
271 at 24 °C and the relative humidity was set to 70%. For the paired group, 2% 4-
272 methycyclohexanol (4-MCH, Sigma-Aldrich, diluted in paraffin oil, Sigma-Aldrich) was
273 presented in a cup with the diameter of 5 mm, together with 12 pulses of electric shocks at
274 90 V for 1 minute inside the training tube. The unpaired group received the same 1-minute
275 electric shock first, followed by 1-minute rest, and then the same 1-minute 4-MCH

276 presentation. Flies were dissected at 3 min, 20 min, 90 min, 270 min and 1 day after
277 conditioning. Experiments were performed multiple times on different days for a single
278 group.
279
280 **Sample preparation**
281 Animals used in experiments involving comparisons between control and experimental
282 groups were dissected on the same day. Data were collected from multiple batches of
283 experiments performed on different days. Flies were anesthetized by ice and placed on ice
284 before dissection. The dissection was performed in cold PBS to collect the brain without
285 the ventral nerve cord. The brains were subsequently fixed by 2% paraformaldehyde for 1 h
286 and then washed 3×20 min by 0.1% PBT (0.1% Triton X-100 in PBS) in a PCR tube,
287 typically 5-6 brains in one tube. Samples were mounted on microscope slides using
288 mounting medium SeeDB2S [65].
289
290 **Confocal microscopy image acquisition**
291 The image acquisition was performed using an Olympus FV1200 confocal microscope
292 platform equipped with both PMT and GaAsP high sensitivity detectors and a 60×/1.42 NA
293 oil immersion objective (PLAPON60XO, Olympus). The Kalman filter was turned on to 2×
294 averaging while scanning. For Brp::rGFP samples in all GAL4 types, scanning speed was
295 set at 2 μs/pixel with a voxel size of lateral 0.079 × 0.079 × axial 0.370 μm. For
296 experimental point spread function (PSF) imaging, SeeDB2S immersed beads were
297 scanned in a setting that is 60×/1.42 NA oil immersion objective; 473 nm laser power:

298 2.0%; 559 nm laser power: 1.5%; voxel size: 0.079 μm × 0.079 μm × 0.370 μm; scanning
299 speed: 4 μs/pixel, to produce multiple bead images.
300

301 **PSF acquisition and image deconvolution**

302 Sub-resolution fluorescent beads (Tetraspeck Microspheres 0.1 μm, Thermo Fisher
303 Scientific, T7279) were imaged to generate the PSF. The bead solution was diluted with
304 distilled water and sonicated several times to eliminate aggregation. PSF images acquired
305 were processed using Amira software (Thermo Fisher Scientific) with the Extract Point
306 Spread Function module. The PSFs extracted from each image were averaged to create a
307 single PSF for later image deconvolution (Resizing voxel size: 0.079 μm × 0.079 μm ×
308 0.370 μm; 32 pixels × 32 pixels × 21 slices of image size). Image deconvolution was
309 performed by using the Richardson-Lucy iterative non-blind algorithm in a Fiji plugin
310 DeconvolutionLab2 [66], or by CLIJ2 GPU-based Richardson-Lucy deconvolution [67]. Images
311 were deconvolved 20 times iteratively to improve image quality.
312

313 **Brp clusters segmentation and data analysis**

314 For Brp::rGFP cluster detection, the image stack size was adjusted to double the XY plate
315 pixel number using Fiji to increase the detection precision. The images were subsequently
316 processed using the 3D maxima finder and the 3D spot segmentation function of the 3D
317 suite package in Fiji. 3D maxima were identified for each cluster and used as the starting
318 point for pixel clustering [36]. An intensity threshold (threshold) and the noise tolerance were
319 set to reduce noise and adjust the sensitivity of 3D maxima detection respectively. The

threshold set the value of all pixels that have values below the threshold to NaN (not a number). The noise tolerance is set in the 3D maxima finder. To be noticed, the threshold is only applied to the image used to find 3D maxima. The 3D maxima finder generates the 3D maxima. The 3D segmentation function then requires the 3D maxima and the raw image, so that there is no intensity cut affecting the measurement of cluster volume (used deconvolved image). The local thresholding method for the 3D segmentation was set to Gaussian fit, with the "SD value" set to 2. Cluster volume was measured as the voxel count within the 3D ROI.

The above procedures may include a tiling and stitching step for images and data because of the limited computer power. Typically, an image was tiled into 25 sub-stacks with overlapped margins. After being processed separately, the data acquired from all tiled sub-stacks was stitched back with a deletion of overlapping data points to generate the complete detection result. Nearest neighbors were identified for each particle and spatial distances in between (NND) were calculated using Python. For each sample, mean NND was calculated separately. For a particular Brp::rGFP cluster, the number of surrounding clusters within r ($r = 3 \times$ mean NND) spherically including itself is referred as the "AZ density". The "local intensity" of a particular Brp::rGFP cluster is the average of Brp::rGFP intensity of all clusters surrounding within r ($r = 3 \times$ mean NND) including itself. The plot function of Python was used to plot the color-coded 3D reconstructed maps.

F-score calculation

The 3D detection parameters were optimized by matching the 3D maxima detection results to the ground truths. Ground truths were defined by annotating AZs manually, according to the size, position and signal pattern of Brp puncta in the images. The F-score was used to assess detection precision. F-score is the harmonic mean of a system's precision and recall value, calculated by the following formula: 2 × [(Precision × Recall) / (Precision + Recall)]. The precision is the number of true positives divided by the total number of identified positives, including incorrect identification. The recall is the number of true positives divided by the total number of true data points defined as the ground truth. F-scores shown in Fig. 1 were automatically calculated using a customized Fiji Marco that aligned 3D maxima with ground truth. Different combinations of noise threshold and noise tolerance were tested for the test images cropped from raw images.

Statistical analysis

Statistical analysis was performed using GraphPad Prism version 8, 9 and 10 or Python. For statistical comparisons, Kruskal-Wallis test with original False Discovery Rate method of Benjamini and Hochberg correction was applied expect as explicitly mentioned. A desired false discovery rate of 0.05. Pearson's correlation coefficient (R) was calculated using Python.

References

1. Kittel, R.J., Wichmann, C., Rasse, T.M., Fouquet, W., Schmidt, M., Schmid, A., Wagh, D.A., Pawlu, C., Kellner, R.R., Willig, K.I., et al. (2006). Bruchpilot Promotes Active Zone

364 Assembly, Ca^{2+} Channel Clustering, and Vesicle Release. Science *312*, 1051–1054.
365 https://doi.org/10.1126/science.1126308.

366 2. Wagh, D.A., Rasse, T.M., Asan, E., Hofbauer, A., Schwenkert, I., Dürrbeck, H.,
367 Buchner, S., Dabauvalle, M.-C., Schmidt, M., Qin, G., et al. (2006). Bruchpilot, a Protein
368 with Homology to ELKS/CAST, Is Required for Structural Integrity and Function of
369 Synaptic Active Zones in Drosophila. Neuron *49*, 833–844.
370 https://doi.org/10.1016/j.neuron.2006.02.008.

371 3. Fouquet, W., Owald, D., Wichmann, C., Mertel, S., Depner, H., Dyba, M., Hallermann,
372 S., Kittel, R.J., Eimer, S., and Sigrist, S.J. (2009). Maturation of active zone assembly by
373 Drosophila Bruchpilot. J Cell Biol *186*, 129–145. https://doi.org/10.1083/jcb.200812150.

374 4. Matkovic, T., Siebert, M., Knoche, E., Depner, H., Mertel, S., Owald, D., Schmidt, M.,
375 Thomas, U., Sickmann, A., Kamin, D., et al. (2013). The Bruchpilot cytomatrix determines
376 the size of the readily releasable pool of synaptic vesicles. J Cell Biol *202*, 667–683.
377 https://doi.org/10.1083/jcb.201301072.

378 5. Paul, M.M., Pauli, M., Ehmann, N., Hallermann, S., Sauer, M., Kittel, R.J., and
379 Heckmann, M. (2015). Bruchpilot and Synaptotagmin collaborate to drive rapid glutamate
380 release and active zone differentiation. Front Cell Neurosci *9*, 29.
381 https://doi.org/10.3389/fncel.2015.00029.

382 6. Akbergenova, Y., Cunningham, K.L., Zhang, Y.V., Weiss, S., and Littleton, J.T. (2018).
383 Characterization of developmental and molecular factors underlying release heterogeneity
384 at Drosophila synapses. Elife *7*, e38268. https://doi.org/10.7554/elife.38268.

385 7. Newman, Z.L., Bakshinskaya, D., Schultz, R., Kenny, S.J., Moon, S., Aghi, K., Stanley,
386 C., Marnani, N., Li, R., Bleier, J., et al. (2022). Determinants of synapse diversity revealed
387 by super-resolution quantal transmission and active zone imaging. Nat Commun *13*, 229.
388 https://doi.org/10.1038/s41467-021-27815-2.

389 8. Zheng, Z., Lauritzen, J.S., Perlman, E., Robinson, C.G., Nichols, M., Milkie, D.,
390 Torrens, O., Price, J., Fisher, C.B., Sharifi, N., et al. (2018). A Complete Electron
391 Microscopy Volume of the Brain of Adult Drosophila melanogaster. Cell *174*, 730-
392 743.e22. https://doi.org/10.1016/j.cell.2018.06.019.

393 9. Scheffer, L.K., Xu, C.S., Januszewski, M., Lu, Z., Takemura, S., Hayworth, K.J., Huang,
394 G.B., Shinomiya, K., Maitlin-Shepard, J., Berg, S., et al. (2020). A connectome and
395 analysis of the adult Drosophila central brain. Elife *9*, e57443.
396 https://doi.org/10.7554/elife.57443.

397 10. Takemura, S., Hayworth, K.J., Huang, G.B., Januszewski, M., Lu, Z., Marin, E.C.,
398 Preibisch, S., Xu, C.S., Bogovic, J., Champion, A.S., et al. (2024). A Connectome of the
399 Male Drosophila Ventral Nerve Cord. https://doi.org/10.7554/elife.97769.1.

400 11. Schlegel, P., Yin, Y., Bates, A.S., Dorkenwald, S., Eichler, K., Brooks, P., Han, D.S.,
401 Gkantia, M., Santos, M. dos, Munnelly, E.J., et al. (2024). Whole-brain annotation and
402 multi-connectome cell typing of Drosophila. Nature *634*, 139–152.
403 https://doi.org/10.1038/s41586-024-07686-5.

404 12. Dorkenwald, S., Matsliah, A., Sterling, A.R., Schlegel, P., Yu, S., McKellar, C.E., Lin,
405 A., Costa, M., Eichler, K., Yin, Y., et al. (2024). Neuronal wiring diagram of an adult brain.
406 Nature *634*, 124–138. https://doi.org/10.1038/s41586-024-07558-y.

407 13. Sachse, S., Rueckert, E., Keller, A., Okada, R., Tanaka, N.K., Ito, K., and Vosshall,
408 L.B. (2007). Activity-Dependent Plasticity in an Olfactory Circuit. Neuron *56*, 838–850.
409 https://doi.org/10.1016/j.neuron.2007.10.035.

410 14. Gilestro, G.F., Tononi, G., and Cirelli, C. (2009). Widespread Changes in Synaptic
411 Markers as a Function of Sleep and Wakefulness in Drosophila. Science *324*, 109–112.
412 https://doi.org/10.1126/science.1166673.

413 15. Fernández, M.P., Berni, J., and Ceriani, M.F. (2008). Circadian Remodeling of
414 Neuronal Circuits Involved in Rhythmic Behavior. PLoS Biol. *6*, e69.
415 https://doi.org/10.1371/journal.pbio.0060069.

416 16. Kremer, M.C., Christiansen, F., Leiss, F., Paehler, M., Knapek, S., Andlauer, T.F.M.,
417 Förstner, F., Kloppenburg, P., Sigrist, S.J., and Tavosanis, G. (2010). Structural Long-Term
418 Changes at Mushroom Body Input Synapses. Curr Biol *20*, 1938–1944.
419 https://doi.org/10.1016/j.cub.2010.09.060.

420 17. Zhang, X., Li, Q., Wang, L., Liu, Z.-J., and Zhong, Y. (2018). Active Protection:
421 Learning-Activated Raf/MAPK Activity Protects Labile Memory from Rac1-Independent
422 Forgetting. Neuron *98*, 142-155.e4. https://doi.org/10.1016/j.neuron.2018.02.025.

423 18. Turrel, O., Ramesh, N., Escher, M.J.F., Pooryasin, A., and Sigrist, S.J. (2022).
424 Transient active zone remodeling in the Drosophila mushroom body supports memory.
425 Curr Biol. https://doi.org/10.1016/j.cub.2022.10.017.

426 19. Mosca, T.J., and Luo, L. (2014). Synaptic organization of the Drosophila antennal lobe
427 and its regulation by the Teneurins. eLife *3*, e03726. https://doi.org/10.7554/elife.03726.

428 20. Gao, R., Asano, S.M., Upadhyayula, S., Pisarev, I., Milkie, D.E., Liu, T.-L., Singh, V.,
429 Graves, A., Huynh, G.H., Zhao, Y., et al. (2019). Cortical column and whole-brain imaging

430 with molecular contrast and nanoscale resolution. Science *363*.
431 https://doi.org/10.1126/science.aau8302.

432 21. Chen, Y., Akin, O., Nern, A., Tsui, C.Y.K., Pecot, M.Y., and Zipursky, S.L. (2014).
433 Cell-type-Specific Labeling of Synapses In Vivo through Synaptic Tagging with
434 Recombination. Neuron *81*, 280–293. https://doi.org/10.1016/j.neuron.2013.12.021.

435 22. Davis, R.L. (2023). Learning and memory using Drosophila melanogaster : a focus on
436 advances made in the fifth decade of research. GENETICS.
437 https://doi.org/10.1093/genetics/iyad085.

438 23. Aso, Y., Hattori, D., Yu, Y., Johnston, R.M., Iyer, N.A., Ngo, T.-T., Dionne, H.,
439 Abbott, L., Axel, R., Tanimoto, H., et al. (2014). The neuronal architecture of the
440 mushroom body provides a logic for associative learning. Elife *3*, e04577.
441 https://doi.org/10.7554/elife.04577.

442 24. Yamagata, N., Ezaki, T., Takahashi, T., Wu, H., and Tanimoto, H. (2021). Presynaptic
443 inhibition of dopamine neurons controls optimistic bias. Elife *10*, e64907.
444 https://doi.org/10.7554/elife.64907.

445 25. Pitman, J.L., Huetteroth, W., Burke, C.J., Krashes, M.J., Lai, S.-L., Lee, T., and
446 Waddell, S. (2011). A Pair of Inhibitory Neurons Are Required to Sustain Labile Memory
447 in the Drosophila Mushroom Body. Curr Biol *21*, 855–861.
448 https://doi.org/10.1016/j.cub.2011.03.069.

449 26. Lin, A.C., Bygrave, A.M., Calignon, A. de, Lee, T., and Miesenböck, G. (2014).
450 Sparse, decorrelated odor coding in the mushroom body enhances learned odor
451 discrimination. Nat Neurosci *17*, 559–568. https://doi.org/10.1038/nn.3660.

452 27. Liu, X., and Davis, R.L. (2009). The GABAergic anterior paired lateral neuron
453 suppresses and is suppressed by olfactory learning. Nat. Neurosci. *12*, 53–59.
454 https://doi.org/10.1038/nn.2235.

455 28. Yu, D., Keene, A.C., Srivatsan, A., Waddell, S., and Davis, R.L. (2005). Drosophila
456 DPM Neurons Form a Delayed and Branch-Specific Memory Trace after Olfactory
457 Classical Conditioning. Cell *123*, 945–957. https://doi.org/10.1016/j.cell.2005.09.037.

458 29. Keene, A.C., Stratmann, M., Keller, A., Perrat, P.N., Vosshall, L.B., and Waddell, S.
459 (2004). Diverse Odor-Conditioned Memories Require Uniquely Timed Dorsal Paired
460 Medial Neuron Output. Neuron *44*, 521–533. https://doi.org/10.1016/j.neuron.2004.10.006.

461 30. Keene, A.C., Krashes, M.J., Leung, B., Bernard, J.A., and Waddell, S. (2006).
462 Drosophila Dorsal Paired Medial Neurons Provide a General Mechanism for Memory
463 Consolidation. Curr Biol *16*, 1524–1530. https://doi.org/10.1016/j.cub.2006.06.022.

464 31. Haynes, P.R., Christmann, B.L., and Griffith, L.C. (2015). A single pair of neurons
465 links sleep to memory consolidation in Drosophila melanogaster. eLife *4*, e03868.
466 https://doi.org/10.7554/elife.03868.

467 32. Waddell, S., Armstrong, J.D., Kitamoto, T., Kaiser, K., and Quinn, W.G. (2000). The
468 amnesiac Gene Product Is Expressed in Two Neurons in the Drosophila Brain that Are
469 Critical for Memory. Cell *103*, 805–813. https://doi.org/10.1016/s0092-8674(00)00183-5.

470 33. Huang, S., Piao, C., Beuschel, C.B., Götz, T., and Sigrist, S.J. (2020). Presynaptic
471 Active Zone Plasticity Encodes Sleep Need in Drosophila. Curr Biol *30*, 1077-1091.e5.
472 https://doi.org/10.1016/j.cub.2020.01.019.

473 34. Kamiyama, D., Sekine, S., Barsi-Rhyne, B., Hu, J., Chen, B., Gilbert, L.A., Ishikawa,
474 H., Leonetti, M.D., Marshall, W.F., Weissman, J.S., et al. (2016). Versatile protein tagging
475 in cells with split fluorescent protein. Nat. Commun. *7*, 11046.
476 https://doi.org/10.1038/ncomms11046.

477 35. Kondo, S., Takahashi, T., Yamagata, N., Imanishi, Y., Katow, H., Hiramatsu, S., Lynn,
478 K., Abe, A., Kumaraswamy, A., and Tanimoto, H. (2020). Neurochemical Organization of
479 the Drosophila Brain Visualized by Endogenously Tagged Neurotransmitter Receptors.
480 Cell Reports *30*, 284-297.e5. https://doi.org/10.1016/j.celrep.2019.12.018.

481 36. Ollion, J., Cochennec, J., Loll, F., Escudé, C., and Boudier, T. (2013). TANGO: a
482 generic tool for high-throughput 3D image analysis for studying nuclear organization.
483 Bioinformatics *29*, 1840–1841. https://doi.org/10.1093/bioinformatics/btt276.

484 37. Ehmann, N., Linde, S. van de, Alon, A., Ljaschenko, D., Keung, X.Z., Holm, T., Rings,
485 A., DiAntonio, A., Hallermann, S., Ashery, U., et al. (2014). Quantitative super-resolution
486 imaging of Bruchpilot distinguishes active zone states. Nat Commun *5*, 4650.
487 https://doi.org/10.1038/ncomms5650.

488 38. Gratz, S.J., Goel, P., Bruckner, J.J., Hernandez, R.X., Khateeb, K., Macleod, G.T.,
489 Dickman, D., and O'Connor-Giles, K.M. (2019). Endogenous tagging reveals differential
490 regulation of Ca2+ channels at single AZs during presynaptic homeostatic potentiation and
491 depression. J Neurosci *39*, 3068–18. https://doi.org/10.1523/jneurosci.3068-18.2019.

492 39. Wu, H., Eno, S., Jinnai, K., Maekawa, Y., Saito, K., Abe, A., Williams, D.W.,
493 Yamagata, N., Kondo, S., and Tanimoto, H. (2024). Octopamine signals coordinate the

494 spatial pattern of presynaptic machineries within individual Drosophila mushroom body
495 neurons. bioRxiv, 2024.12.02.626512. https://doi.org/10.1101/2024.12.02.626512.

496 40. Schlegel, P., Yin, Y., Bates, A.S., Dorkenwald, S., Eichler, K., Brooks, P., Han, D.S.,
497 Gkantia, M., Santos, M. dos, Munnelly, E.J., et al. (2023). A consensus cell type atlas from
498 multiple connectomes reveals principles of circuit stereotypy and variation. bioRxiv,
499 2023.06.27.546055. https://doi.org/10.1101/2023.06.27.546055.

500 41. Mrestani, A., Pauli, M., Kollmannsberger, P., Repp, F., Kittel, R.J., Eilers, J., Doose, S.,
501 Sauer, M., Sirén, A.-L., Heckmann, M., et al. (2021). Active zone compaction correlates
502 with presynaptic homeostatic potentiation. Cell Rep. *37*, 109770.
503 https://doi.org/10.1016/j.celrep.2021.109770.

504 42. Ghelani, T., Escher, M., Thomas, U., Esch, K., Lützkendorf, J., Depner, H., Maglione,
505 M., Parutto, P., Gratz, S., Matkovic-Rachid, T., et al. (2023). Interactive nanocluster
506 compaction of the ELKS scaffold and Cacophony Ca2+ channels drives sustained active
507 zone potentiation. Sci. Adv. *9*, eade7804. https://doi.org/10.1126/sciadv.ade7804.

508 43. Vogt, K., Schnaitmann, C., Dylla, K.V., Knapek, S., Aso, Y., Rubin, G.M., and
509 Tanimoto, H. (2014). Shared mushroom body circuits underlie visual and olfactory
510 memories in Drosophila. Elife *3*, e02395. https://doi.org/10.7554/elife.02395.

511 44. Davidson, A.M., Kaushik, S., and Hige, T. (2023). Dopamine-Dependent Plasticity Is
512 Heterogeneously Expressed by Presynaptic Calcium Activity across Individual Boutons of
513 the Drosophila Mushroom Body. eNeuro *10*, ENEURO.0275-23.2023.
514 https://doi.org/10.1523/eneuro.0275-23.2023.

515 45. Bilz, F., Geurten, B.R.H., Hancock, C.E., Widmann, A., and Fiala, A. (2020).
516 Visualization of a Distributed Synaptic Memory Code in the Drosophila Brain. Neuron
517 *106*, 963-976.e4. https://doi.org/10.1016/j.neuron.2020.03.010.

518 46. Perisse, E., Yin, Y., Lin, A.C., Lin, S., Huetteroth, W., and Waddell, S. (2013).
519 Different Kenyon Cell Populations Drive Learned Approach and Avoidance in Drosophila.
520 Neuron *79*, 945–956. https://doi.org/10.1016/j.neuron.2013.07.045.

521 47. Amin, H., Apostolopoulou, A.A., Suárez-Grimalt, R., Vrontou, E., and Lin, A.C.
522 (2020). Localized inhibition in the Drosophila mushroom body. Elife *9*, e56954.
523 https://doi.org/10.7554/elife.56954.

524 48. Sachidanandan, D., Aravamudhan, A., Mrestani, A., Nerlich, J., Lamberty, M.,
525 Hasenauer, N., Ehmann, N., Pauls, D., Seubert, T., Maiellaro, I., et al. (2023). Rab3
526 mediates cyclic AMP-dependent presynaptic plasticity and olfactory learning. bioRxiv,
527 2023.12.21.572589. https://doi.org/10.1101/2023.12.21.572589.

528 49. Eckstein, N., Bates, A.S., Champion, A., Du, M., Yin, Y., Schlegel, P., Lu, A.K.-Y.,
529 Rymer, T., Finley-May, S., Paterson, T., et al. (2024). Neurotransmitter classification from
530 electron microscopy images at synaptic sites in Drosophila melanogaster. Cell *187*, 2574-
531 2594.e23. https://doi.org/10.1016/j.cell.2024.03.016.

532 50. Wu, C.-L., Shih, M.-F.M., Lee, P.-T., and Chiang, A.-S. (2013). An Octopamine-
533 Mushroom Body Circuit Modulates the Formation of Anesthesia-Resistant Memory in
534 Drosophila. Curr Biol *23*, 2346–2354. https://doi.org/10.1016/j.cub.2013.09.056.

535 51. Lee, P.-T., Lin, H.-W., Chang, Y.-H., Fu, T.-F., Dubnau, J., Hirsh, J., Lee, T., and
536 Chiang, A.-S. (2011). Serotonin–mushroom body circuit modulating the formation of
537 anesthesia-resistant memory in Drosophila. Proc. Natl. Acad. Sci. *108*, 13794–13799.
538 https://doi.org/10.1073/pnas.1019483108.

539 52. Davie, K., Janssens, J., Koldere, D., Waegeneer, M.D., Pech, U., Kreft, Ł., Aibar, S.,
540 Makhzami, S., Christiaens, V., González-Blas, C.B., et al. (2018). A Single-Cell
541 Transcriptome Atlas of the Aging Drosophila Brain. Cell *174*, 982-998.e20.
542 https://doi.org/10.1016/j.cell.2018.05.057.

543 53. Zeng, J., Li, X., Zhang, R., Lv, M., Wang, Y., Tan, K., Xia, X., Wan, J., Jing, M.,
544 Zhang, X., et al. (2023). Local 5-HT signaling bi-directionally regulates the coincidence
545 time window for associative learning. Neuron *111*, 1118-1135.e5.
546 https://doi.org/10.1016/j.neuron.2022.12.034.

547 54. Hiramatsu, S., Saito, K., Kondo, S., Katow, H., Yamagata, N., Wu, C.-F., and
548 Tanimoto, H. (2024). Cell-type-specific fluorescent tagging of endogenous target proteins
549 reveals synaptic enrichment and dynamic regulations of dopamine receptors.
550 https://doi.org/10.7554/elife.98358.1.

551 55. Aso, Y., Siwanowicz, I., Bräcker, L., Ito, K., Kitamoto, T., and Tanimoto, H. (2010).
552 Specific Dopaminergic Neurons for the Formation of Labile Aversive Memory. Curr Biol
553 *20*, 1445–1451. https://doi.org/10.1016/j.cub.2010.06.048.

554 56. Liu, C., Plaçais, P.-Y., Yamagata, N., Pfeiffer, B.D., Aso, Y., Friedrich, A.B.,
555 Siwanowicz, I., Rubin, G.M., Preat, T., and Tanimoto, H. (2012). A subset of dopamine
556 neurons signals reward for odour memory in Drosophila. Nature *488*, 512–516.
557 https://doi.org/10.1038/nature11304.

558 57. Aso, Y., and Rubin, G.M. (2016). Dopaminergic neurons write and update memories
559 with cell-type-specific rules. Elife *5*, e16135. https://doi.org/10.7554/elife.16135.

560 58. Yamagata, N., Ichinose, T., Aso, Y., Plaçais, P.-Y., Friedrich, A.B., Sima, R.J., Preat,
561 T., Rubin, G.M., and Tanimoto, H. (2015). Distinct dopamine neurons mediate reward

562 signals for short- and long-term memories. Proc National Acad Sci *112*, 578–583.
563 https://doi.org/10.1073/pnas.1421930112.

564 59. Aso, Y., Herb, A., Ogueta, M., Siwanowicz, I., Templier, T., Friedrich, A.B., Ito, K.,
565 Scholz, H., and Tanimoto, H. (2012). Three Dopamine Pathways Induce Aversive Odor
566 Memories with Different Stability. PLoS Genet. *8*, e1002768.
567 https://doi.org/10.1371/journal.pgen.1002768.

568 60. Burke, C.J., Huetteroth, W., Owald, D., Perisse, E., Krashes, M.J., Das, G., Gohl, D.,
569 Silies, M., Certel, S., and Waddell, S. (2012). Layered reward signalling through
570 octopamine and dopamine in Drosophila. Nature *492*, 433–437.
571 https://doi.org/10.1038/nature11614.

572 61. Baltruschat, L., Prisco, L., Ranft, P., Lauritzen, J.S., Fiala, A., Bock, D.D., and
573 Tavosanis, G. (2021). Circuit reorganization in the Drosophila mushroom body calyx
574 accompanies memory consolidation. Cell Reports *34*, 108871.
575 https://doi.org/10.1016/j.celrep.2021.108871.

576 62. Tirian, L., and Dickson, B.J. (2017). The VT GAL4, LexA, and split-GAL4 driver line
577 collections for targeted expression in the Drosophila nervous system. bioRxiv, 198648.
578 https://doi.org/10.1101/198648.

579 63. Stocker, R.F., Heimbeck, G., Gendre, N., and Belle, J.S. de (1997). Neuroblast ablation
580 in Drosophila P[GAL4] lines reveals origins of olfactory interneurons. J. Neurobiol. *32*,
581 443–456. https://doi.org/10.1002/(sici)1097-4695(199705)32:5<443::aid-neu1>3.0.co;2-5.

582 64. Pfeiffer, B.D., Jenett, A., Hammonds, A.S., Ngo, T.-T.B., Misra, S., Murphy, C.,
583 Scully, A., Carlson, J.W., Wan, K.H., Laverty, T.R., et al. (2008). Tools for neuroanatomy
584 and neurogenetics in Drosophila. Proc. Natl. Acad. Sci. *105*, 9715–9720.
585 https://doi.org/10.1073/pnas.0803697105.

586 65. Ke, M.-T., Nakai, Y., Fujimoto, S., Takayama, R., Yoshida, S., Kitajima, T.S., Sato,
587 M., and Imai, T. (2016). Super-Resolution Mapping of Neuronal Circuitry With an Index-
588 Optimized Clearing Agent. Cell Reports *14*, 2718–2732.
589 https://doi.org/10.1016/j.celrep.2016.02.057.

590 66. Sage, D., Donati, L., Soulez, F., Fortun, D., Schmit, G., Seitz, A., Guiet, R., Vonesch,
591 C., and Unser, M. (2017). DeconvolutionLab2: An open-source software for deconvolution
592 microscopy. Methods *115*, 28–41. https://doi.org/10.1016/j.ymeth.2016.12.015.

593 67. Haase, R., Royer, L.A., Steinbach, P., Schmidt, D., Dibrov, A., Schmidt, U., Weigert,
594 M., Maghelli, N., Tomancak, P., Jug, F., et al. (2020). CLIJ: GPU-accelerated image

processing for everyone. Nat. Methods *17*, 5–6. https://doi.org/10.1038/s41592-019-0650-1.

Acknowledgments

We thank all lab members of Tanimoto Lab at Tohoku University for valuable discussions.

We thank Dr. Yuki Tsukada at Keio University for crucial advice on Fiji-based image analysis.

We thank Vienna Drosophila Resource Center and Bloomington Drosophila Stock Center for transgenic flies.

Funding:

Ministry of Education, Culture, Sports, Science and Technology 22H05481 (HT)

Ministry of Education, Culture, Sports, Science and Technology 22KK0106 (HT)

Ministry of Education, Culture, Sports, Science and Technology 20H00519 (HT)

Japan Science and Technology Agency JPMJSP2114 (HW)

Tohoku University Research Program 'Frontier Research in Duo' (HT).

Author contributions:

Conceptualization: HW, HT

Methodology: HW, YM, NY, SE, SK

Investigation: HW, YM, SE

Visualization: HW, SE

Resources: SK

Supervision: HW, NY, HT

Writing—original draft: HY, HT

Writing—review & editing: HW, SE, HT

Competing interests

Authors declare that they have no competing interests.

Data and materials availability

Further information and requests on resources and reagents should be directed to and will be fulfilled by the corresponding author, Dr. Hiromu Tanimoto (hiromut@m.tohoku.ac.jp). This study did not generate any unique code. All data needed to evaluate the conclusions in the paper are present in the paper.

Figures and Tables

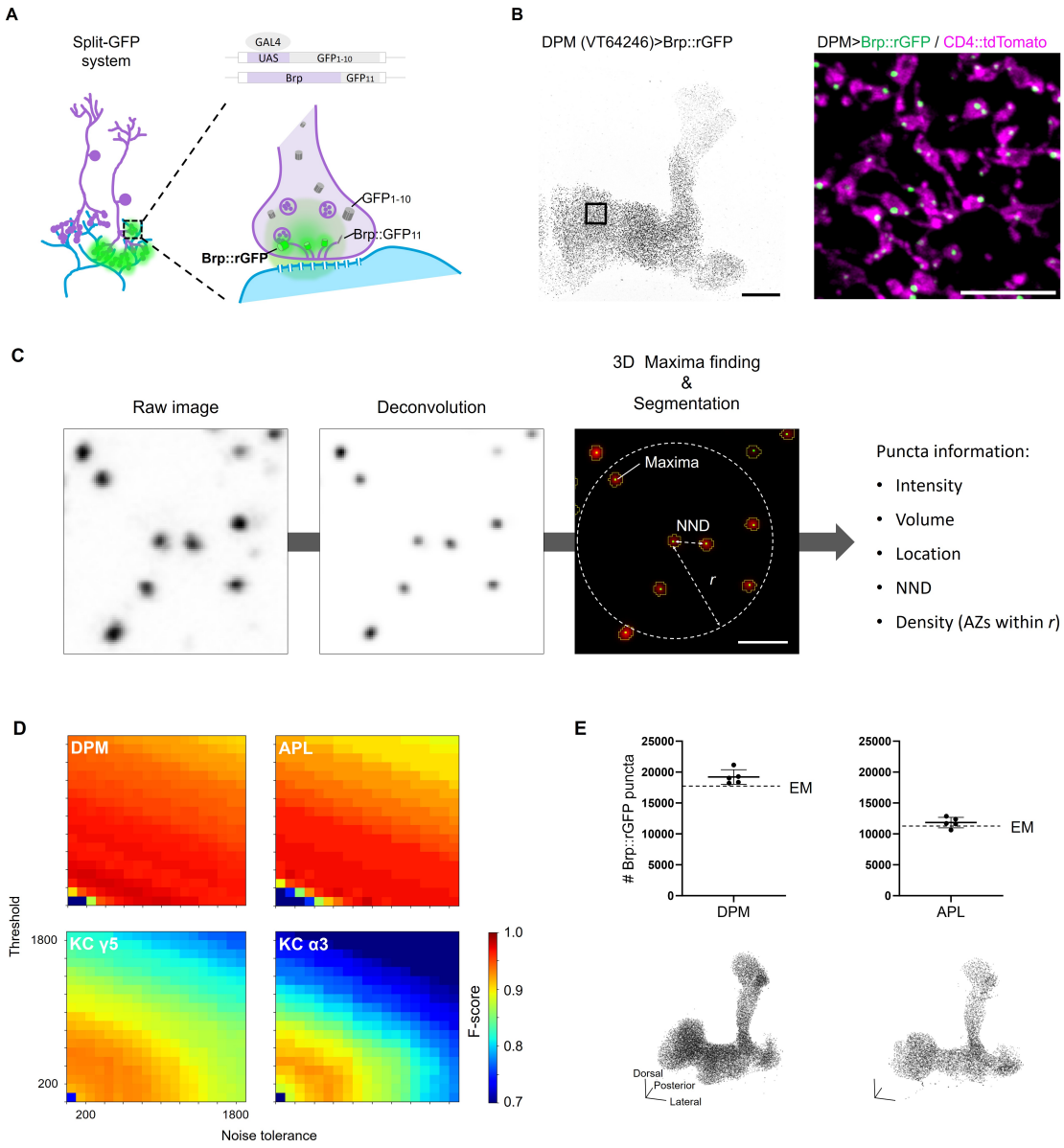

Fig. 1. Spatial characterization of Brp::rGFP clusters at single-AZ level.

(**A**) Schematic of the split-GFP tagging strategy. The GFP_{11} fragment is inserted by CRISPR/Cas9 just prior to the stop codon of *brp*, while GFP1-10 is expressed in specific cell types via GAL4-UAS system.

636 (**B**) Brp::rGFP signals in DPM. The entire MB lobe structure is shown. The black box in
637 the left panel indicates the zoom-in area (right panel). GFP1-10 and CD4::tdTomato
638 (magenta) were co-expressed using *VT64246-GAL4*. Scale bar, 20 μm (left); 5 μm (right).
639 (**C**) Image processing pipeline. Raw images were processed with image deconvolution to
640 improve the signal quality. 3D maxima (green pixels) are detected for each Brp::rGFP
641 cluster. Pixels around the maxima were clustered to created 3D ROIs, indicated by yellow
642 circles. The "AZ density" is the number of Brp::rGFP clusters within r (3 × mean NND).
643 Scale bar, 1 μm.
644 (**D**) Heatmaps of F-scores showing the detection performance across in different cell types.
645 An intensity threshold (threshold) is applied to reduce the background noise when detecting
646 3D maxima. The noise tolerance is the parameter that adjusts the sensitivity of 3D maxima
647 detection. The color represents the F-score value.
648 (**E**) Number of Brp::rGFP clusters detected in DPM and APL. The dashed lines indicate the
649 number of electron dense projections identified in the hemibrain connectome for DPM
650 (17530) and APL (10789) on the MB lobes and peduncle (cite the resource here). For both
651 DPM and APL, n = 5. Lower panels show the representative 3D reconstructions of
652 Brp::rGFP clusters in DPM and APL. Scale bars, 20 μm. Data were presented as mean ±
653 s.e.m.

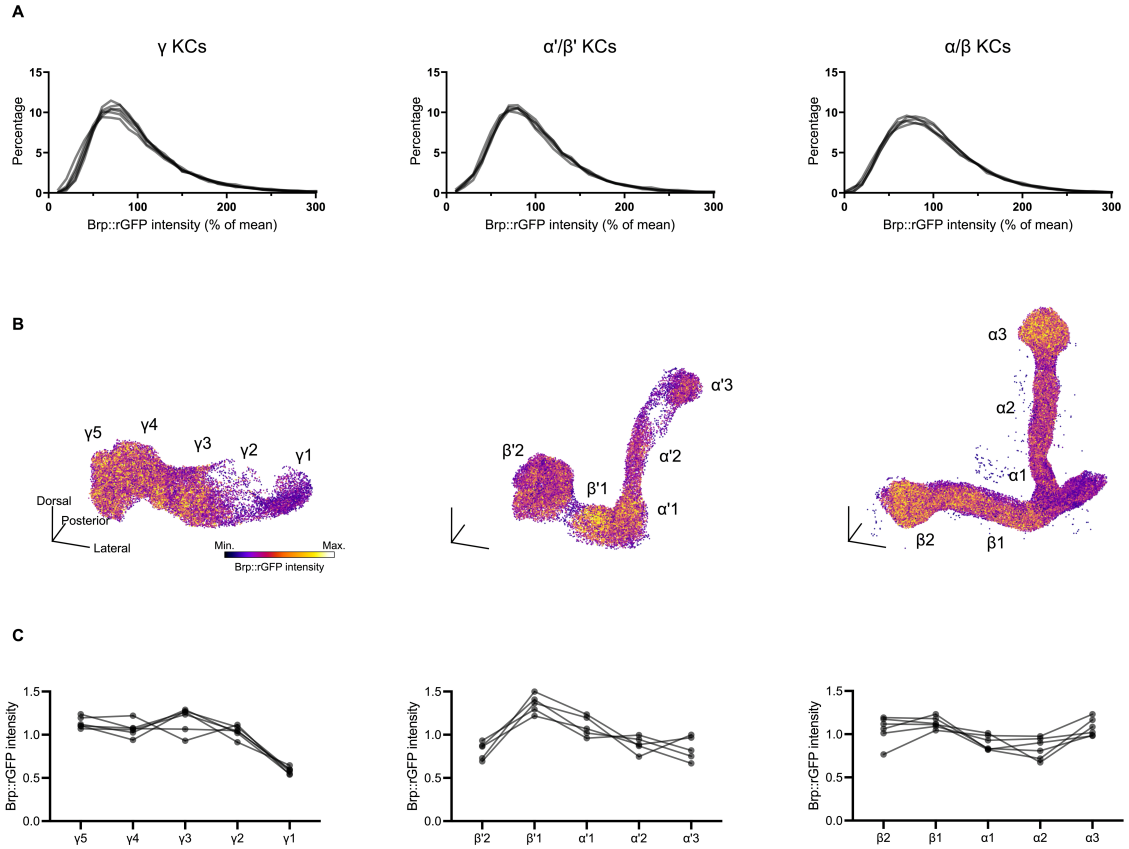

654

655 **Fig. 2. Compartmentalized AZ structures of KCs.**

656 (**A**) Histograms of the signal intensity of individual Brp::rGFP clusters from three KC

657 subtypes. Values are normalized by the mean intensity in each data set (each sample). Each

658 line represents the histogram of one independent sample. γ KCs (*MB009B-GAL4*), n = 6;

659 α/β KCs (*MB370B-GAL4*), n = 5; α'/β' KCs (*MB008B-GAL4*), n = 5.

660 (**B**) 3D reconstructions of Brp::rGFP clusters in three KC subtypes, colored by the

661 Brp::rGFP intensity. The approximate locations of compartments are as indicated. Min. and

662 Max. were set to represent the lowest and highest 5% of Brp::rGFP intensity value in the

663 dataset respectively. Scale bars, 20 μm.

664 (C) Signal intensity of Brp:rGFP clusters in each compartment. Brp::rGFP puncta were
665 quantified compartmentally. Medians in different compartments are showed as the ratio
666 against the average of five compartments in the corresponding KC subtype. Each line
667 represents one independent sample.

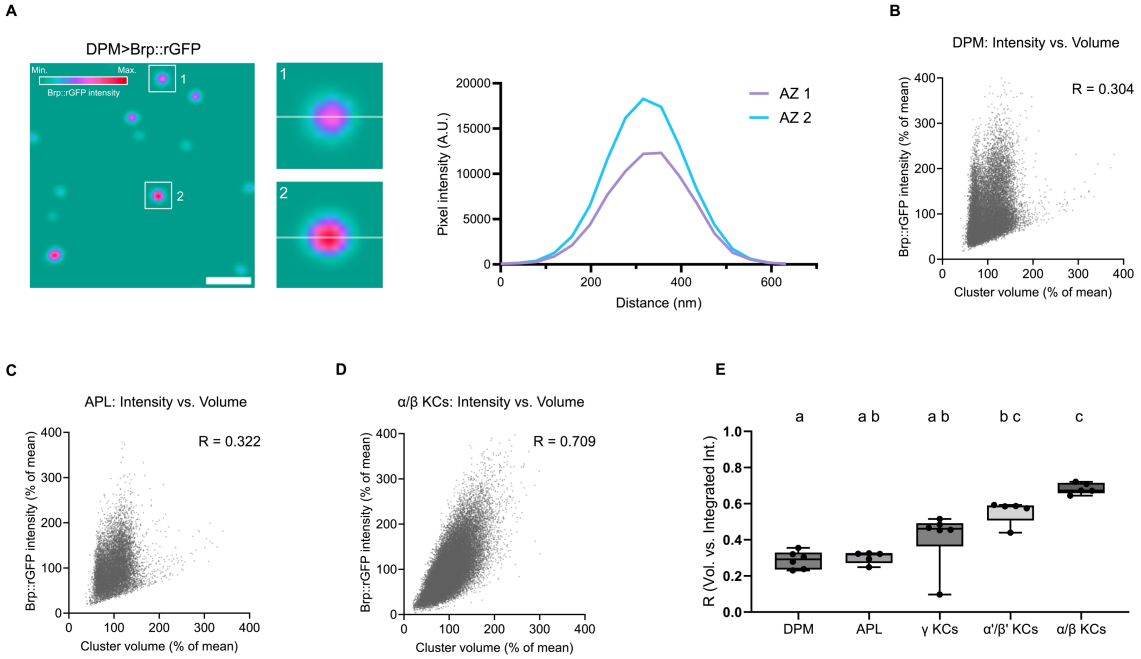

Fig. 3. The variability of Brp::rGFP concentrations depends on cell type.

(**A**) Brp::rGFP clusters with distinct intensities but similar size in DPM. The left panel shows a cropped image of Brp::rGFP in DPM. White boxes indicate areas zoomed-in in panels 1 and 2. Transparent white lines in panels 1 and 2 show the lines on which the intensity profiles were plotted. Intensity profiles were plotted for AZ1 (magenta) and AZ2 (blue) respectively.

(**B-D**) Scatter plots showing the correlation between the Brp::rGFP intensity and cluster volume in DPM, APL and α/β KCs. Data of three representative samples were shown. Pearson correlation coefficient R were calculated for each sample.

(**E**) Correlations between the intensity and volume of Brp::rGFP clusters in different cell types. DPM (n = 6), APL (n = 5), γ KCs (n = 6, *MB009B-GAL4*), α'/β' KCs (n = 5, *MB370B-GAL4*), α/β KCs (n = 5, *MB008B-GAL4*). DPM vs. α'/β' KCs: P = 0.0253; DPM

681 vs. α/β KCs: P = 0.0009; APL vs. α/β KCs: P = 0.0035; γ KCs vs. α/β KCs: P = 0.0418.

682 Values marked with different lowercase letters represent significant difference ($P < 0.05$);

683 Data were presented as box plots showing center (median), whiskers (Min. to Max.).

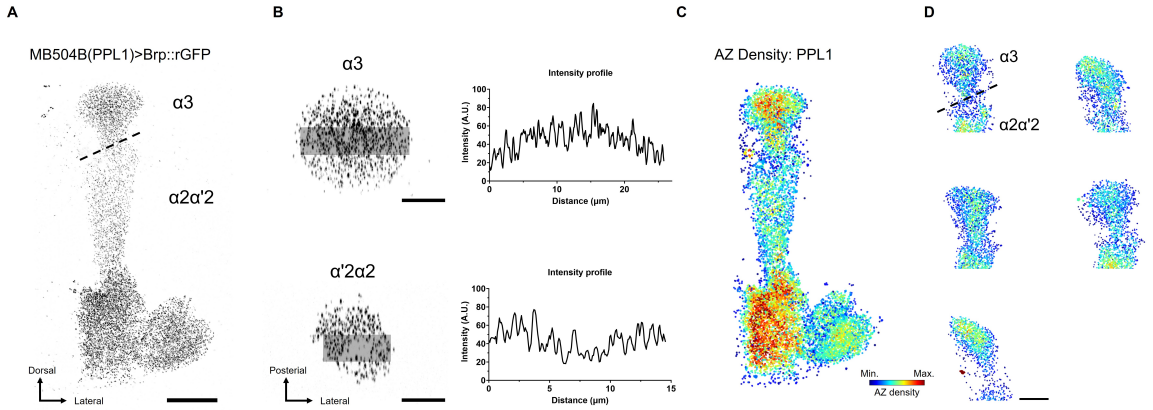

684

685 **Fig. 4. Stereotyped AZ distribution of PPL1-α3 DAN.**

686 (**A**) Brp::rGFP in PPL1 DANs. UAS-GFP$_{1\text{-}10}$ was expressed using *MB504B-GAL4*. Dashed

687 line marks the rough boundary between α3 and α2α'2 compartments. Scale bar, 20 μm.

688 (**B**) Brp::rGFP intensity profiles of α3 and α2α'2 compartments. Left panels show the max-

689 projection images of α3 and α2α'2 optical coronal sections. Transparent gray stripes

690 indicate areas where intensity profiles are plotted in the right panels. Scale bars, 10 μm.

691 (**C**) 3D reconstruction colored by the AZ density in PPL-1 DANs. Color scale: Min. = 0,

692 Max. = 40. Dashed line indicates the rough boundary between α3 and α2α'2 compartments.

693 Scale bar, 20 μm.

694 (**D**) Stereotyped AZ distribution pattern in PPL1-α3 across individuals. 3D reconstructions

695 show the AZ density across different brain samples. Scale bar, 20 μm.

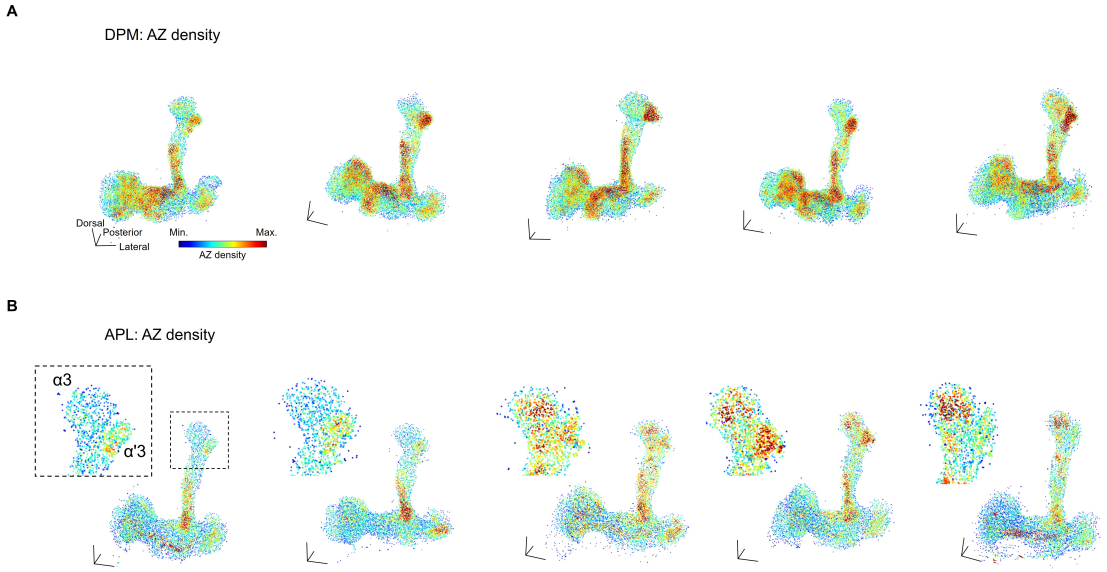

696

697 **Fig. 5. Cell-type-specific stereotypy of AZ spatial distributions.**

698 (**A**) 3D reconstructions of Brp::rGFP clusters in DPMs, colored by AZ density. Color scale:

699 Min. = 0, Max. = 35. Black arrows indicate consistently high AZ density regions across

700 brain samples. Scale bars, 20 μm.

701 (**B**) 3D reconstructions of Brp::rGFP clusters in APLs, colored by AZ density. Color scale:

702 Min. = 0, Max. = 30. Black dashed square indicates the area zoomed-in. APL

703 reconstructions are arranged from left to right according to the overall AZ density in α3.

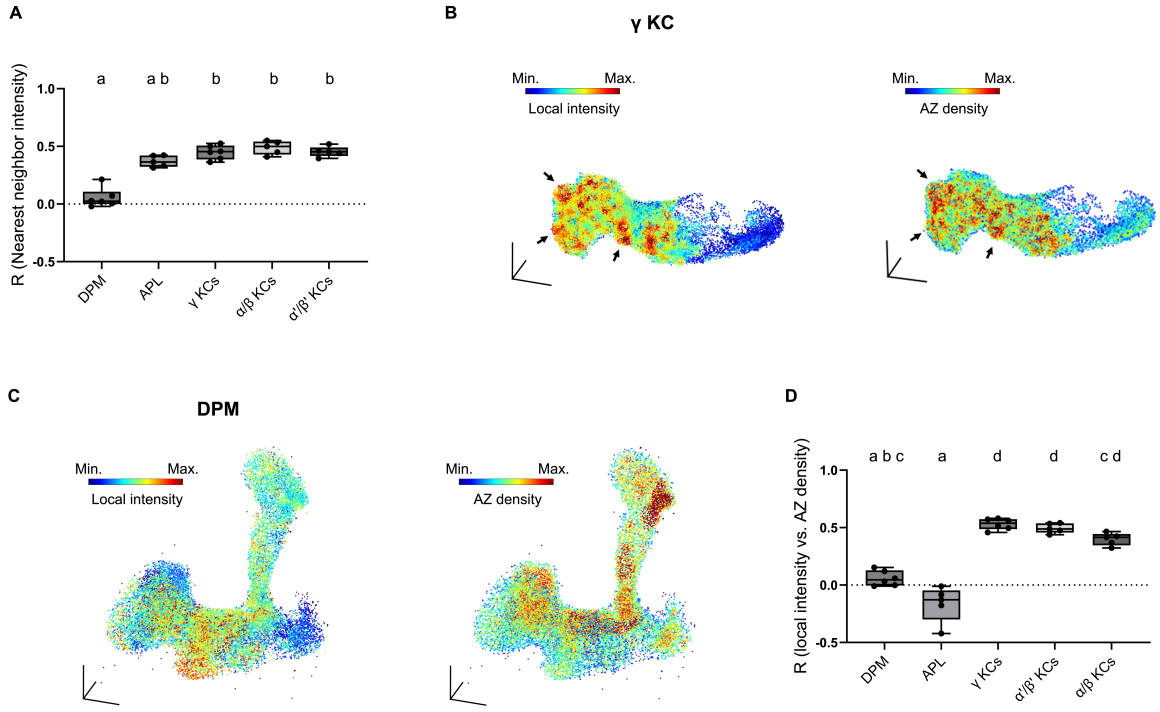

Fig. 6. Local intensity analysis revealed sub-compartmental AZ structures.

(**A**) Correlation of Brp::rGFP intensities between nearest neighbor AZs in different cell types. Brp::rGFP intensities were log transformed. DPM vs. γ KCs: P = 0.0066; DPM vs. α'/β' KCs: P = 0.0027; DPM vs. α/β KCs: P = 0.0066; Scale bar: 1 μm.

(**B**) 3D reconstructions of Brp::rGFP clusters in a γ KC sample, colored by local intensity and AZ density. Black arrows indicate areas with both high local intensities and high AZ densities. Min. and Max. were set to represent the lowest and highest 5% in local intensity value respectively. Color scale of AZ density: Min. = 0 and Max = 35.

(**C**) 3D reconstructions of Brp::rGFP clusters in a DPM neuron, colored by local intensity and AZ density. Min. and Max. are set to represent the lowest and highest 5% in local intensity value respectively. Color scale of AZ density: Min. = 0, Max. = 35.

716 (**D**) Correlations between AZ density and local intensity in different cell types. DPM (n =

717 6), APL (n = 5), γ KCs (n = 6, *MB009B-GAL4*), α'/β' KCs (n = 5, *MB370B-GAL4*), α/β KCs

718 (n = 5, *MB008B-GAL4*). DPM vs. γ KCs: P = 0.0171; DPM vs. α'/β' KCs: P = 0.0171; APL

719 vs. γ KCs: P = 0.0014; APL vs. α'/β' KCs: P = 0.0014; APL vs. α/β KCs: P = 0.0171.

720

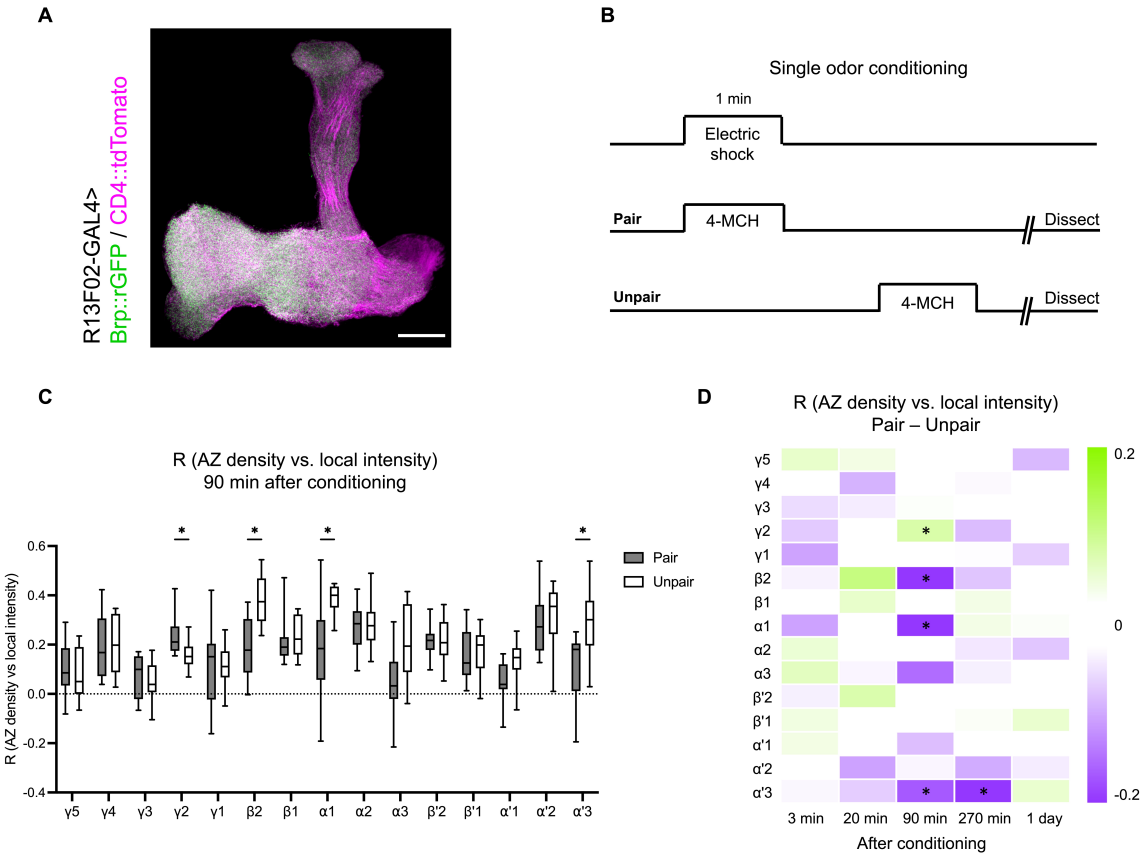

Fig. 7. Associative conditioning re-organizes sub-compartmental active zone clusters.

(A) Brp::rGFP (green) and CD4::tdTtomato cytoplasm membrane marker (magenta) in KCs, visualized by using *R13F02-GAL4*.

(B) The experimental design of the aversive single odor conditioning. Files in the pair group receive concurrent presentation of 2% 4-MCH and 90 V electric shock. Flies in the unpair group first receive the electric shock first and then 4-MCH 1 min later. Flies were dissected at different time points after the conditioning.

(C) Correlation coefficient (AZ density vs. local intensity of individual Brp::rGFP puncta) of each compartment at 90 min after conditioning. Pair (n = 11) vs. Unpair (n = 12), γ2 (P = 0.0261), β2 (P = 0.0060), α1 (P = 0.0026), α'3 (P = 0.0026).

732 (D) Heatmap showing the difference of correlation coefficient (AZ density vs. local
733 intensity of Brp::rGFP puncta) between the pair and unpair group at different time points
734 after conditioning. The color indicates the difference and the asterisks in the compartments
735 indicate the significant difference. For 3 min, Pair (n = 12), Unpair (n = 11); For 20 min,
736 Pair (n = 12), Unpair (n = 11); For 90 min, Pair (n = 11) vs. Unpair (n = 12), P = 0.0247;
737 For 270 min, Pair (n = 11), Unpair (n = 11), ; For 1 D, Pair (n = 12), Unpair (n = 9);
738 For all results involved statistical comparison, only significant results are shown. Scale
739 bars, 20 μm. Mann-Whitney test with original False Discovery Rate (FDR) method of
740 Benjamini and Hochberg correction. *P<0.05. Data were presented as box plots showing
741 centre (median), whiskers (Min. to Max.).
742